Electrochemical performance of two-dimensional Ti_3C_2-Mn_3O_4 nanocomposites and carbonized iron cations for hybrid supercapacitor electrodes

Kabir O. Oyedotun[1], Damilola Y. Momodu[1], Michael Naguib[2], Abdulmajid A. Mirghni[1], Tshifhiwa M. Masikhwa[1], Abubakar A. Khaleed[1], Mesfin Kebede[3], and Ncholu Manyala[1]*

[1]Department of Physics, Institute of Applied Materials, SARCHI Chair in Carbon Technology and Materials, University of Pretoria, Pretoria 0028, South Africa.
[2]Department of Physics and Engineering Physics, Tulane University, New Orleans, LA 70118, USA.
[3]Energy Materials, Materials Science and Manufacturing, Council for Scientific and Industrial Research (CSIR), Pretoria, 0001, South Africa
*Corresponding author's email: ncholu.manyala@up.ac.za, Tel.: + (27)12 420 3549.

Highlights

- High performance Ti_3C_2—Mn_3O_4 nanocomposite is synthesis via solvothermal process.
- Characterization of the nanocomposite is obtained using various techniques.
- A synergy of features is achieved by integrating Mn_3O_4 into Ti_3C_2 network.
- An assembled hybrid Ti_3C_2—Mn_3O_4//C-FP device yields comparable energy density.

Abstract

In this work, we present a simple two-step synthesis route to develop a cost effective high performance Ti_3C_2-Mn_3O_4 nanocomposite via a solvothermal process at 150 °C. The characterization of the composite material was obtained via various techniques. Electrochemical performance study of the material as a potential supercapacitor electrode demonstrated a maximum specific capacity of 128 mAh g^{-1} at a specific current of 1 A g^{-1} in a 6 M KOH aqueous electrolyte. A capacity retention of 77.7% of the initial value was recorded after over 2,000 galvanostatic cycles at 10 A g^{-1} for the single electrode. More so, the as-prepared nanocomposite sample electrode also showed a relatively stable property with an energy efficiency of 83.5 % after cycling tests. Interestingly, an assembled hybrid supercapacitor device with carbonized iron cations (C-FP) and the Ti_3C_2-Mn_3O_4 composite delivered a specific capacity of 78.9 mAh g^{-1}. The device yielded a high energy of 28.3 Wh kg^{-1} with an equivalent 463.4 W kg^{-1} power densityat 1 A g^{-1}. A good cycling stability performance with an energy efficiency of 90.2% in addition to a 92.6% capacity retention was observed for over 10,000 cycles at specific current of 3 A g^{-1} over a voltage window of 1.5 V.

KEYWORDS: MXene, Ti_3C_2-Mn_3O_4, nanocomposites, specific capacity, supercapacitor electrodes, carbonized iron cations.

1. Introduction

As a result of higher demand for cleaner energy being witnessed globally, there is an urgent need to further explore novel clean energy sources and associated energy storage systems to work efficiently in storing the as-generated energy [1,2]. Electrochemical capacitors, the recent innovative energy storage components has gained much research attention due to their demonstrated potential to not only be used in combination with the much older battery technology framework but also additional merits such as its environmentally friendliness, high power densities (fast charge/discharge abilities) and long cycle life [2,3].

Various materials have been examined as electrodes for energy storage devices, such as activated carbon, metal hydroxides/oxides, metal sulfides and conducting polymers with efforts being focused on the exploration of novel composite electrode materials to enhance electrochemical performance of the supercapacitor device via exploitation of the individual material storage capability [4,5].

Until the separation of mono layer graphene in 2004 [6], two-dimensional (2D) materials have caught great research attention owing to their characteristic attributes connected to their bulk form. There are currently numerous new 2D materials, some of which are transition metal dichalcogenides, transition metal sulphides, and transition metal oxides, among others [7–10]. MXenes are a new class of 2D materials, which were recently discovered to be applicable in most dynamic and technologically advancing applications. It mainly exists as transitional metal nitrides and/or carbides having a common formula $M_{n+1}X_nT_z$, where M, X, and T_z are the early transition metal elements, nitrogen and/or carbon , and surface limiting groups (mainly OH, O, and F), respectively, with n = 1, 2, or 3 [11,12].

The 2D materials have hydrophilic surfaces [13] with high metallic conductivities usually around6000 to 8000 Scm^{-1} [14], which confirms its suitable accomplishment in energy storage devices applications, catalysis, water desalination, electromagnetic interference shielding, and conducting thin films [14–18] among others [13]. The materials have attracted significance attention basically for their enormous potential in applications such as energy storage devices which include electrochemical capacitors and metal-ion batteries [12,19,20].

Till to date, the significance of MXenes, viz., early transition metal carbides and/or carbonitrides, is currently vastly investigated by researchers globally for further energy storage applications, which is obtainable based on its good electrical conductivities and surface terminations which makes it electrochemically active [1,13,21].

Manganese oxide (Mn_3O_4) in the form of hausmannite is a black mineral. It is composed of a spinel structure, having tetragonal distortion arising from a Jahn-Teller effect on the Mn^{+2} ion. The tetrahedral and octahedral sites of the Mn^{+2} $(Mn^{+3})_2O_4$ structure are occupied by the Mn^{+2} and Mn^{+3} ions respectively. The hausmannite material in its tetragonal crystal structure has lattice parameters a = 0.5762 nm, b = 0.5762 nm, and c = 0.9470 nm with space group $I4_1/amd$ [22]. Manganese oxides of different structures have also been widely adopted as electrode materials, soft magnetic materials, and catalysts [23–27], of which Mn_3O_4 is popular as a top catalyst material for redox reactions in general. For instance, the material is known for its use as a catalyst in selective reduction of nitrobenzene and methane and carbon monoxide oxidation process the [24]. Mn_3O_4 is mainly produced by calcination of manganese hydroxides, hydroxyoxides, or oxysalts at a temperature usually above 800 °C. Its nanowires could be produced via the hydroxide powder calcination at 850 °C using the micro-emulsion technique [24,28]. Generally, Mn_3O_4 particles synthesized using these traditional

methods possess low surface area and with random shape thereby limiting their specific uses. The materials specific physical and chemical attributes account for their suitability as catalysis and energy storage devices applications among others [24]. Nevertheless, Mn_3O_4 is intrinsically poor in electrical conductivity hence incorporating nanostructured Mn_3O_4 into conductive 2D carbon-based materials has been recently explored by other researchers [29],[30–32].

Based on the available reports involving the incorporation of these pseudocapacitive oxide materials with other electrically conductive carbon-based materials, it is expected that Mn_3O_4 insertion into the electrically conductive $Ti_3C_2T_z$ layers will generally be considered as a promising approach to further solve the poor electrical conductivity property. By maximizing the conductive and flexible characteristic of the $Ti_3C_2T_z$ layers as the scaffold material, Mn_3O_4 nanoparticles could be uniformly dispersed between the $Ti_3C_2T_z$ layers to facilitate ionic and electronic transport. The issue of restacking of the nanolayers could also be limited with the presence of the embedded Mn_3O_4 nanoparticles.

In this work, a binder-free $Ti_3C_2T_z$-Mn_3O_4 nanocomposite electrode has been fabricated via a green solvothermal process. This process permits for an exact influence on the magnitude, form, as well as crystallinity of metal oxide nanostructures. A synergy of the individual electrochemical features of these materials is achieved by integrating the Mn_3O_4 into the Ti_3C_2 network. Besides, the nature of the composites assembled was a free-standing film without the use of binders which further increased the rate kinetics and system stability [30]. The Mn_3O_4 lying on the surface of the $Ti_3C_2T_z$ layers could improve the active material-electrode surface contact which will in turn smoothen the process of electrons transfer to the current collector, thereby remarkably improving the electrochemical accomplishment of the entire composite material as electrode.

2. Experimental

2.1. Materials preparation

2.1.1. Preparation of the $Ti_3C_2T_z$ (MXene) material

The $Ti_3C_2T_z$ utilized for the synthesis of the $Ti_3C_2T_z$-Mn_3O_4 nanocomposite material was synthesized as reported in earlier work [21,33]. Briefly, the Ti_3AlC_2 powder was synthesized by ball-milling equal molar ratio of Ti_2AlC and TiC powders for 4 h with the aid of zirconia balls, With the resulting mixture been heated to 1350 °C for 2 h in argon gas flow. The recovered sample was crushed with a pestle, in a mortar. About 10 g of Ti_3AlC_2 powder (-325 mesh) was then dispersed in 100 mL of a 48% concentrated HF aqueous solution at 25 °C for 18 h. The recovered suspension was washed severally with fresh deionized (DI) water, centrifuged to remove the etching products and remaining acids until the pH reached values > 4. Then the powders were separated from the liquid using vacuum-assisted filtration device.

2.1.2. Preparation of Mn_3O_4 nanoparticles

0.768 g of $KMnO_4$ was dispersed in 100 mL ethanol (99.9 %) and 0.5 mL of 10.2 M HCl was added drop-wise upon magnetic stirring at 25 °C to achieve a uniform mixture. The contents were then transferred into a Teflon-lined autoclave for a dwelling time of 4 hours at a temperature of 150 ˚C. The system was left to cool down naturally, and the recovered sample was washed severally with DI water to be free of excess reagent. The brown precipitate was then dried for 12 h in an electric oven at 60 ˚C in air (under normal laboratory conditions).

2.1.3. Preparation of $Ti_3C_2T_z$-Mn_3O_4 nanocomposite

100 mg $Ti_3C_2T_z$ was dispersed in 100 mL ethanol 99.9 % upon magnetic stirring at room temperature with subsequent sonication for 1 h to speed-up uniform dispersion. Thereafter, 0.768 g $KMnO_4$ was added to the $Ti_3C_2T_z$ mixture with a drop-wise introduction of 0.5 mL HCl (10.2 M) for homogeneity while magnetically stirring the entire reaction chamber for nearly 30 minutes. The resulting mixture was poured into a Teflon-lined stainless steel autoclave unit, bubbled with argon gas to prevent oxidation of the sample before being sealed and heated up to 150 ˚C for a dwelling time of 4 h. After been left to cool down naturally, the precipitated sample was washed severally with DI water until a pH 7 was recorded and then oven dried at 60 ˚C for 12 h in air to obtain the $Ti_3C_2T_z$-Mn_3O_4 nanocomposite (see scheme 1).

Scheme 1: Diagram of the synthesis process of $Ti_3C_2T_z$-Mn_3O_4 nanocomposite.

2.1.4. Preparation of carbonized iron cations (C-FP) electrode

The carbonized Iron cations used as the negative electrode in the fabrication of the Ti_3C_2-Mn_3O_4//C-FP hybrid supercapattery device was prepared as depicted in our earlier work [34,35]. Briefly, the iron-containing mixture, C-FP was pyrolysed by entirely dissolving $Fe(NO_3)_2$. $9H_2O$ salt in ethanol, with subsequent addition of Polyaniline (PANI) already reported in our earlier work [34]. The resulting mixture was put into

sonication until slurry that was pasted onto nickel foam template. The prepared sample was later moved into a Quartz tube and annealed at 850 °C for 2 h under N_2 atmosphere for the iron cations (Fe^{3+}) to be adsorbed onto the PANI film directly grown onto the nickel foam template.

2.2. Materials characterization

The as-synthesized samples micrographs and energy dispersive X-ray (EDX) spectrum were acquired using a Zeiss Ultra Plus 55 field emission scanning electron microscope (FE-SEM) actuated at 1.0 kV, alongside with a JEOL JEM 2100F high-resolution transmission electron microscope (HRTEM FEI Tecnai-F30) operated with a 200 KV acceleration voltage. X-ray diffraction (XRD) analysis was achieved by using an XPERT-PRO diffractometer (PANalytical BV, Netherlands) having a reflection geometry at 2θ values of 9–90° and a step size of 0.01°, actuating with a Co Kα radiation source (λ = 0.178901 nm). An alpha 300 RAS+ Confocal micro-Raman spectrometer (WiTec Focus Innovations, Germany) set on the 532 nm laser wavelength was employed to analyze the as-prepared samples with a spectral acquisition time of 150 s and laser power of 5 mW. Fourier transform-infrared (FT-IR) analysis was achieved via a Varian FT-IR spectroscopy in a range of 500-4000 cm^{-1} in wavenumber, while the X-ray photoelectron spectroscopy (XPS) analysis was achieved with the help of a Physical Electronics Versa Probe 5000 spectrometer activated with a 100 µm monochromatic Al-Kα exciting source. The textural properties of the samples were acquired by using a Micrometrics TriStar II 3020 pore analyzer run in the range 0.01–1.0 of relative pressure (P/Po), with a pre-degassing done under vacuum for 18 h at 100 °C. Brunauer-Emmett-Teller (BET) and Barrett–Joyner–Halenda (BJH) models were utilized to ascertain the specific surface area (SSA) as well as pore size distribution (PSD) of the samples respectively. Thermogravimetry analysis (TGA) measurements of the as-prepared

samples were done by using a thermogravimetric analyzer, TGA-STA 449C between 20 °C and 1000 °C at 20 °C/min in air. XRF analysis of the compacted powder nanocomposite was carried out by using the ARL Perform'X Sequential XRF instrument with Uniquant software for examination.

2.3. Electrochemical measurements

The electrode materials were fabricated by muddling the active material (90 wt. %) with conductive carbon (10 wt. %) and N-methyl-2-pyrrolidone (NMP) to make slurry. The prepared slurry was pasted onto a 1.0 X 1.0 cm^2 area of the annealed nickel foam template serving as the current collector with subsequent drying at 60 °C overnight. Afterwards, the as-synthesized electrodes were subjected to a pressure of 20 MPa for about 20 seconds. A Bio-Logic VMP300 potentiostat (Knoxville TN 37930, USA) was employed to measure the capacitive performance of the nickel foam-supported electrodes via a three-electrode electrochemical set-up. The performance assessments were carried out using a counter electrode made of glassy carbon, an Ag/AgCl/3 M KCl reference electrode, and the active materials on nickel foam stubs serving as the working electrodes in 6 M KOH at 25 °C. The areal loading mass of each of the active materials was estimated to be nearly 2.5, 2.1, 2.1 and 2.6 mg cm^{-2} for the $Ti_3C_2T_z$-Mn_3O_4, $Ti_3C_2T_z$, Mn_3O_4 and C-FP electrodes correspondingly.

Cyclic voltammetry (CV) tests of the as-synthesized $Ti_3C_2T_z$, Mn_3O_4, $Ti_3C_2T_z$-Mn_3O_4 samples were performed at distinct scan rates ranging from 5 to 100 mV s^{-1} within a negative and a positive operating potential windows of -0.4 to -0.9 V and 0.0 to 0.35 V vs. Ag/AgCl correspondingly. The galvanostatic charge-discharge (GCD) measurement was done at various increasing specific currents from 1 to 10 A g^{-1}. The electrochemical impedance spectroscopy (EIS) was carefully measured in an open-circuit potential, in a frequency range of 10 mHz to 100 kHz.

The single electrode specific capacity, Q_s (mAh g^{-1}) was obtained via the CV profiles using the relation depicted in equation 1below:

$$Q_s = \frac{1}{3.6*mS_c}\int_{E_1}^{E_2} I * EdE \quad (1)$$

where, E_1 and E_2 are the peak potentials, I (mA) is the current response, E (V) is the electrode potential, S_c (mV s^{-1}) as the scan rate, and m (g) is mass of the active material.

The reliable specific capacity, Q_s(mAh g^{-1}) and energy efficiency, η_E (%) of the materials were acquired by the adoption of a more accurate GCD technique and estimated via the curves at distinct specific currents in line with the following relations expressed as [36]:

$$Q_s = \frac{I\Delta t}{3.6m} \quad (2)$$

$$\eta_E = \frac{E_d}{E_c} \times 100 \quad (3)$$

From equations 2 and 3 above, *I* (mA) typifies the discharge current, *t* measured in seconds is the time taken for a complete discharge cycle, and *m* measured in grams accounts for the mass of the electrode. η_E is the energy efficiency, E_d represents the discharge energy, while E_c is the charge energy obtained by integrating the area under the CD profiles respectively.

The asymmetric hybrid device referred to as supercapattery was assembled by adopting the fabricated Ti_3C_2-Mn_3O_4 nanocomposite as positive electrode, and the C-FP material as negative electrode in a standard 2032 grade coin-type cell using a Watman Celgard paper-based as separator. The overall area mass loading of both Ti_3C_2-Mn_3O_4 and C-FP active material components in the hybrid device was calculated to be nearly 3.37 mg/cm^2, with an electrode thickness of around 91 µm estimated via microbalance,

and a diameter of ~ 1.4 cm. Performance evaluation of the asymmetric device was performed in a two-electrode configuration using 6 M KOH aqueous electrolyte.

Equations 4 and 5 stated below were adopted for the estimation of both energy and power densities for the hybrid supercapattery, (Ti_3C_2-Mn_3O_4//C-FP) from the area under the discharge curve:

$$E_d = I/3.6m \int V dt \quad [\text{Wh kg}^{-1}] \tag{4}$$

$$P_d = 3600 \times E_d/\Delta t \ [\text{W kg}^{-1}] \tag{5}$$

I describes the discharge current (A), *m* (g) represents mass of active material. The integral term is the area under the CD curve and Δ*t* in seconds are the potential window as well as electrode discharge time respectively, and $E_d \ and P_d$, are energy and power densities sequentially.

To our notice, the assembled hybrid asymmetry supercapacitor (SC) operates well in a larger potential window, *c.a.* 1.50 Volts. For best output, respective mass of each electrode in the device was balanced according to the law, $Q_+ = Q_-$, and the charge stored on each electrode depicted as:

$$Q = Q_s \times m \, \Delta E \tag{6}$$

In equation 6, *Q* measured in coulombs (C) represents the charge stored on the electrode, while Q_s *in* mAh g^{-1} typifies the specific capacity estimated on the basis of mass of the active material. ΔE (V) is the electrode potential, and *m* (g) as the mass of active material.

The precise mass equilibrium between the two (positive and negative) electrodes was calculated using a more expression of $Q_+ = Q_-$ as:

$$\frac{m_+}{m_-} = \frac{Q_{s-}\ \Delta E_-}{Q_{s+}\ \Delta E_+} \quad (7)$$

3. Results and discussions

3.1. Morphological, structural and compositional analysis

Fig. 1 demonstrates the FESEM images of the as-prepared materials. Fig. 1 (a-b) presents the surface morphology of the Ti_3C_2 sample at both low and high magnifications respectively. It is evident that the as-prepared Ti_3C_2 is made up of stacked sheet-like structure similar to that of exfoliated graphite or transition metal oxides [37]. The as-observed image confirms the successful removal of the aluminum layer through the HF treatment resulting in a stacked Ti_3C_2 accordion-like morphology which could enhance the electrode/electrolyte contact thereby resulting in efficient ionic transport and pseudo-capacitance performance [1].

Fig. 1 (c-d) displays the FESEM micrographs of Mn_3O_4 material at low and high magnifications accordingly. It could be noticed that the material is composed majorly of tiny, agglomerated irregular nanoparticles that have probably been constituted by the aggregation of smaller Mn_3O_4 nanostructures [38].

Fig. 1 (e-f) displays the FESEM images of Ti_3C_2-Mn_3O_4 composite at various magnifications. It can be observed that the addition of Mn_3O_4 leads to its integration in-between the Ti_3C_2 sheets giving the Ti_3C_2-Mn_3O_4 nanocomposite mix. In addition, the Ti_3C_2 nanosheets function as a conductive support base for the aggregated Mn_3O_4 nanostructures which will likely serves as a nanoscale collector for electron transfer [1,39].

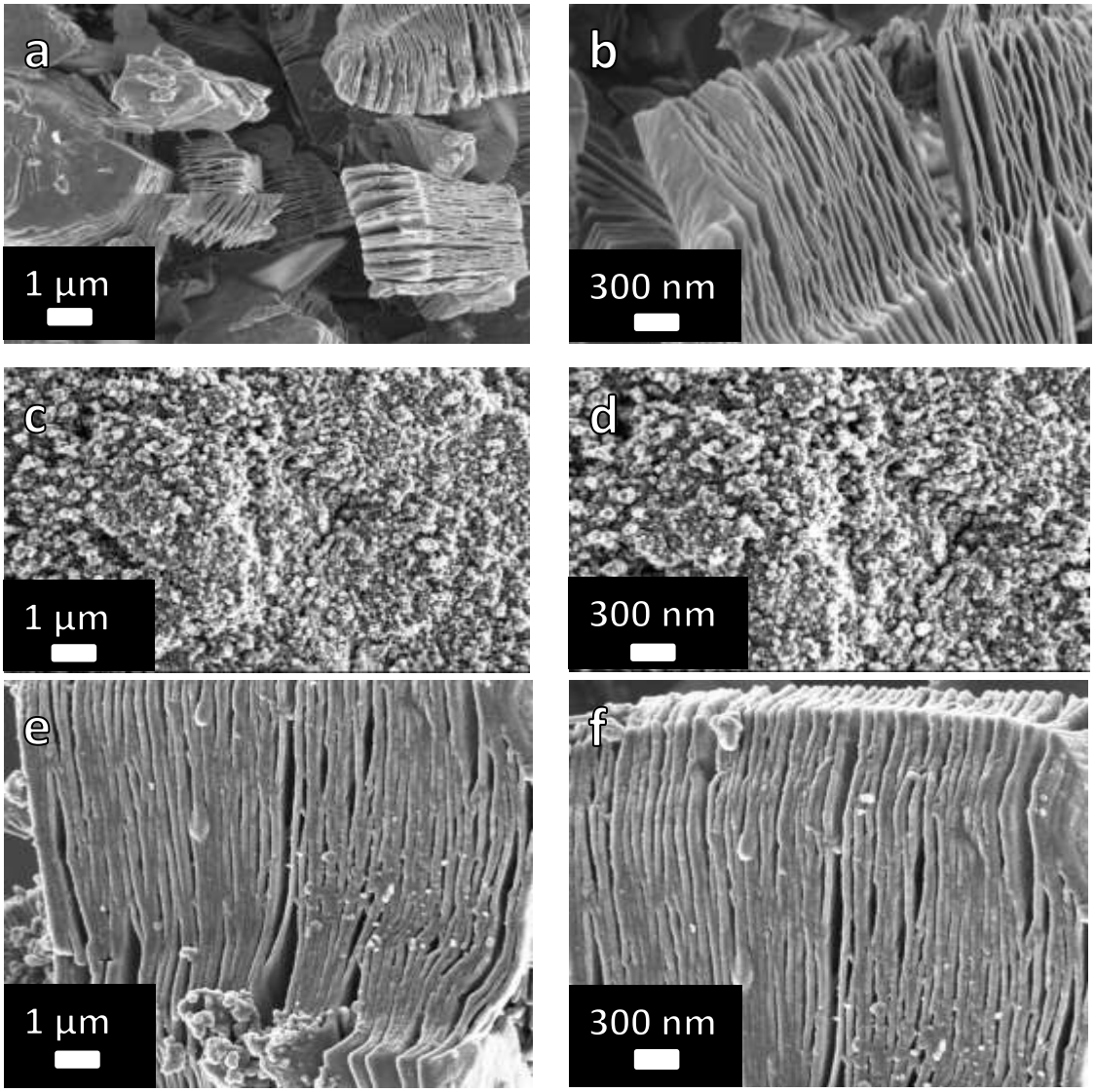

Fig. 1. SEM images of (a-b) the pristine Ti_3C_2, (c-d) the pristine Mn_3O_4 and (e-f) Ti_3C_2-Mn_3O_4 hybrid at low and high magnifications respectively.

Fig. 2 (a-b) indicates the HRTEM images of the Mn_3O_4 sample portraying uniformly distributed irregular nanoparticles which agrees well with SEM results from Fig. 1 (c–d). Fig. 2 (c-d) demonstrates a characteristic HRTEM micrograph of the Ti_3C_2-Mn_3O_4 nanocomposite electrode material indicating the fine layered structure of the material. The interlayer spacing of the material was estimated to be ~ 12.51-18.64 nm as shown in Fig. 2(c). The Mn_2O_3 nanostructures are obviously seen located in the interlayer spacing of the MXene sheets along with some located on the surfaces as indicated with

the arrows in Fig. 2 (d). It can also be noticed that the Ti_3C_2 nanosheets are evenly loaded with numerous Mn_3O_4 nanoparticles as shown in Fig. 2d with an approximate thickness of ~ 7.89-10.25 nm.

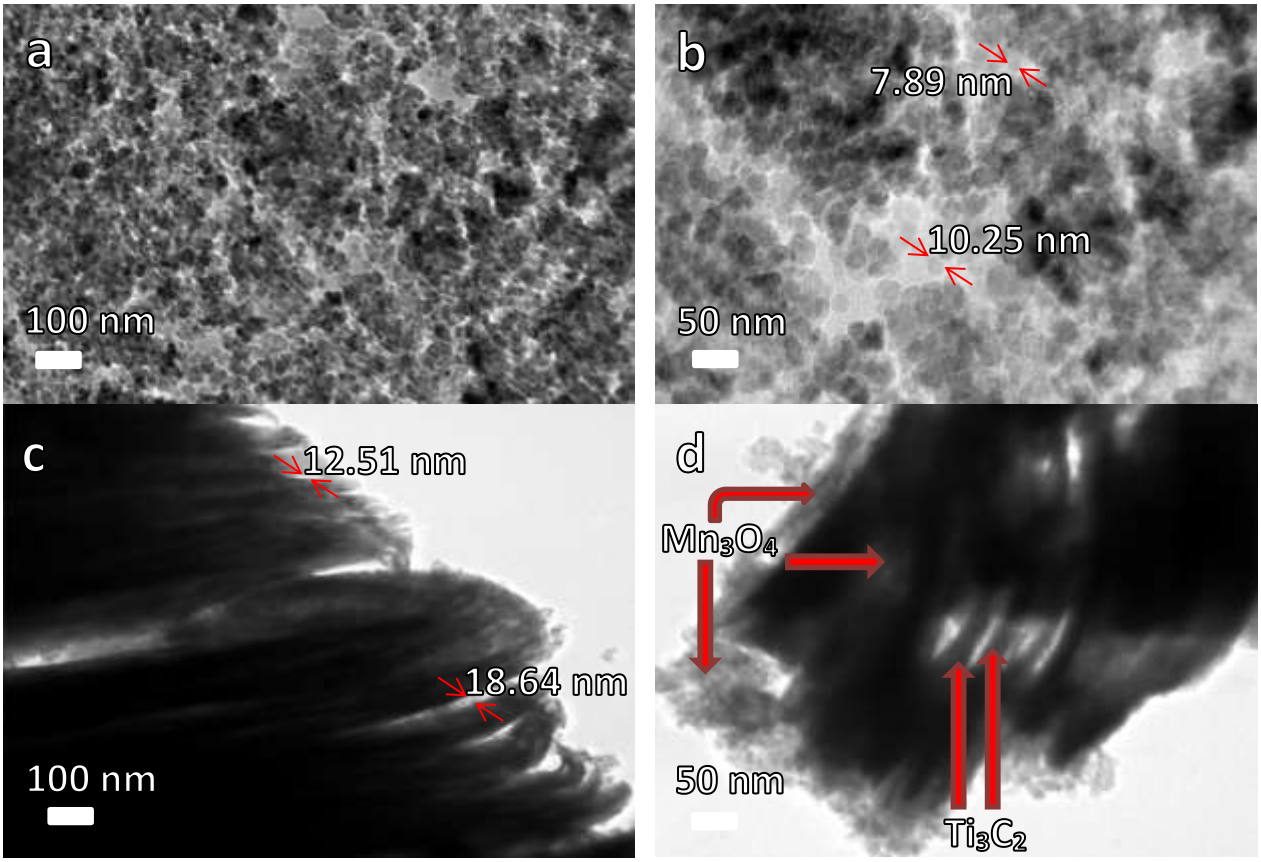

Fig. 2. HRTEM images of (a-b) Mn_3O_4 and (c-d) Ti_3C_2-Mn_3O_4 nanocomposite at low and high magnifications respectively.

Fig. 3 (a) shows the XRD spectra of Ti_3C_2, Mn_3O_4, and Ti_3C_2-Mn_3O_4 composite. There exist peaks at 2θ values of about 10° (d-spacing; 5.15201 Å), 20.8° (d-spacing; 4.91807 Å) and 32° (d-spacing; 3.08401 Å) which correspond to (002), (006) and (008) planes of a pure Ti_3C_2 material earlier reported by other researchers [3,21,40].

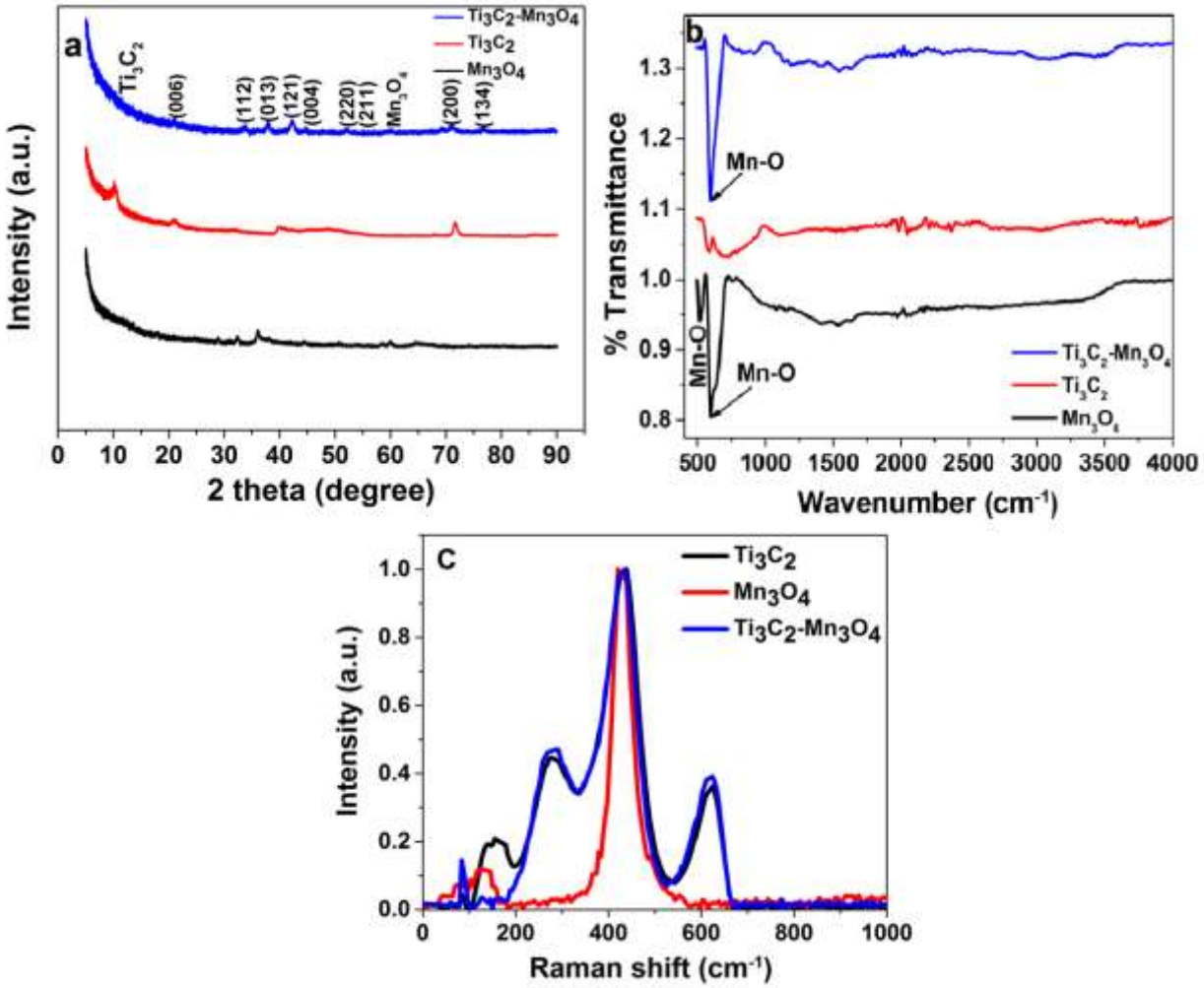

Fig.3. (a) XRD patterns, (b) FTIR spectra and (c) Raman spectra of the as-prepared Ti_3C_2 pristine, Mn_3O_4 pristine and Ti_3C_2-Mn_3O_4 nanocomposite respectively.

The broad and low intensity (002) peak at 2θ = 10° arises from the larger *d*-spacing due to the structural expansion from HF etching as well as Al substitution with -F and the -OH/=O bonding groups. The broad peak observed at approx. 39.6° (104) is typical of the 2D $Ti_3C_2T_x$ MXene materials [41]. The diffraction pattern of Mn_3O_4 shows strong peaks corresponding to (101), (112), (211), (220), (204), (015) and (400) planes ascribed to the hausmannite Mn_3O_4 tetragonal structure indexed according to JCPDS card No. 00-24-0734. The intense peaks from the XRD pattern of the Ti_3C_2-Mn_3O_4 nanocomposite corresponding to both Ti_3C_2 and Mn_3O_4 indicated that the Ti_3C_2-Mn_3O_4 nanocomposite was properly synthesized.

Fourier transform infrared spectroscopy (FTIR) was performed to examine the surface functional groups. The FTIR spectra of the Ti_3C_2, Mn_3O_4 and Ti_3C_2-Mn_3O_4 are shown in Fig. 3 (b). The two strong transmission peaks around 601 and 520 cm^{-1} can be designated to the combined mode connecting Mn-O stretching modes of tetrahedral and octahedral sites in Mn_3O_4. However, in the Mn_3O_4 spectrum, the bands around 1630 and 1400 cm^{-1} are characteristics of resonances of the surface adsorbed O-H molecules and carbonate ions that are present with Mn atoms proportionally in atmosphere. In addition, the spectrum for the nanocomposite material recorded peaks around 596 and 515 cm^{-1} which can also be observed for Mn_3O_4 spectrum, indicating the presence of Mn_3O_4 in the nanocomposite. For all the samples, the peaks around 3400 and 1520 cm^{-1} are known to be an attribute of strongly hydrogen-bonded (–OH) groups or external water molecules been absorbed on the surface. Therefore, the accomplished coating of Mn_3O_4 nanoparticles on the Ti_3C_2 sheets is further confirmed by the FTIR results.

Fig. 3 (c) demonstrates the Raman spectra of Ti_3C_2, Mn_3O_4, and Ti_3C_2-Mn_3O_4 nanocomposites in the 100–2000 cm^{-1} region. Raman spectroscopy peaks of the as-prepared Ti_3C_2 samples at around 150, 275, 435, and 623 cm^{-1} are consistent with that of the reported data in the literature [38,42]. The observed peaks at around 275, 360, and the strong peak centered at 655 cm^{-1} are characteristic features of the tetragonal Mn_3O_4 structure [38], which conform with the XRD analysis in Fig. 3 (a). The Ti_3C_2-Mn_3O_4 nanocomposite Raman spectrum shows strong peaks at around 275, 434, and 623 cm^{-1} indicating the successful synthesis of Ti_3C_2-Mn_3O_4 nanocomposite.

Fig. S1 (*see supporting information*) shows the elemental and chemical analysis of Ti_3C_2-Mn_3O_4 nanocomposite. Fig. S1 (a) shows the EDX spectrum, while Fig. S1 (b) depicts a table of the chemical analysis for the as-synthesized Ti_3C_2-Mn_3O_4 nanocomposite respectively. From the Fig., it is evident that the nanocomposite material

is mainly made up of C, O, Ti and Mn. The material reveals traces of Cl and Si which could be linked to the resin used in the EDX substrate sample preparation, and the F contents is ascribed to the HF etching step employed in the Ti_3C_2 MXenes preparation. Fig. S2 displays the nitrogen adsorption–desorption isotherms obtained from the analysis and used in evaluating the BET surface area alongside with the pore size distribution of Ti_3C_2-Mn_3O_4 nanocomposite. The results indicate an increase in the SSA after deposition of the Mn_3O_4 material (*see Fig. S2 (a) in the supporting information*).

A BET SSA of 37.0 $m^2\ g^{-1}$ was recorded for the synthesized nanocomposite material compared to that of the pristine Ti_3C_2 sample (5.5 $m^2\ g^{-1}$). The improved SSA was ascribed to the integration of numerous Mn_3O_4 nanoparticles into the interlayer spaces between the Ti_3C_2 sheets resulting in an enlargement of pore sites after the solvothermal process. Fig. S2 (b) displays the corresponding pore-size distribution (PSD) plots of the pristine MXene material and the Ti_3C_2-Mn_3O_4 composite confirming the presence of mesopores within structure of the material [1]. From the PSD plots, the presence of both micropores and mesopores is confirmed within both materials with a peak centered at ca. 2.0 nm and a higher volume of mesopores recorded between 3.0 – 4.5 nm. Furthermore, the introduction of Mn_3O_4 nanoparticles into the Ti_3C_2 nanosheets provides larger SSA and more mesopores for cation intercalation which is also indicated with the higher pore volume displayed for the Ti_3C_2-Mn_3O_4 nanocomposite. This unique layered pore structure in the composites could improve the material's charge storage performance when applied as supercapacitor electrodes [43].

The thermal stability of the Ti_2C_3, Mn_3O_4 and the Ti_2C_3-Mn_3O_4 samples was evaluated by thermogravimetric analysis (TGA) performed in air between 20 °C and 1000 °C as shown in Fig. S2 (c) in the supporting information. From the TGA profile, a very slight weight loss close to a 100 °C temperature point was observed which was related to the

loss of interfacial-adsorbed moisture in both Mn_3O_4 and Ti_2C_3-Mn_3O_4 samples. The weight loss just below 300 °C was asserted to the evaporation of adsorbed water molecules [44,45]. The TGA profile of the oxidized Ti_3C_2 was observed to depict two processes which contribute to the weight change. The weight gains at around 420 ˚C is attributed to the Ti_3C_2 (MXene) oxidation, forming titanium dioxide and carbon [47].

The corresponding weight loss is due to the carbon combustion with further heating [46,47]. From the residual weights of the two samples (90.10% (Mn_3O_4) and 57.23% (Ti_3C_2-Mn_3O_4)) at 994 °C, the Mn_3O_4 contents in the composites materials was estimated to be ~32.87 wt%.

Fig. S3 (*see supporting information*) portrays the surface elemental composition of the as-synthesized Ti_3C_2-Mn_3O_4 sample analyzed further using the XPS technique. The high resolution XPS survey scans exhibited the presence of Mn, Ti, O and C atoms.

Fig. S3 (a) shows the Mn*2p* core level peaks with a $2p_{3/2}$–$2p_{1/2}$ doublet at 639.2 eV and 650.8 eV coupled with a spin-splitting width of 11.626 eV in the Mn 2*p* spectrum which is in accordance with the spectrum for Mn_3O_4 [48,49]. The peaks observed at 639.2 eV and 650.8 eV are ascribed to Mn $2p_{3/2}$ and Mn $2p_{1/2}$, correspondingly. This binding energy corresponds to the oxidation state of Mn(II) and Mn(III).

Fig. S3 (b) shows the Ti 2p core levels with doublets (Ti 2p3/2 and Ti 2p1/2) at 455.770 and 461.5 eV respectively coupled with a splitting width of 5.7 eV which agrees well with earlier studies reported in the literature [50,51].

Fig. S3 (c) shows the deconvoluted C*1s* peaks with the main C-C bond recorded at a binding energy of 282.0 eV, and other associated bonds like the C-O bonds and the C=O bonds observed at 283.2 eV and 286.0 eV binding energies respectively [52].

Fig. S3 (d) shows the deconvoluted O*1s* core level peaks. The peak conprises two components at 529.2 eV (a characteristic of metal-oxygen bonds) and at 527.3 eV which could be linked to the lattice oxygen in the material and the oxygen of the hydroxide ions respectively [53,54].

A molar ratio of 5:1 was obtained for the Mn_3O_4:Ti_2C_3 in the composite material using XRF method and is depicted in Table S1 in the supporting document. The ARL Perform'X Sequential XRF instrument with Uniquant software was employed for the analysis of elements in the periodic table in interval of Na and U, with just the elements discovered over the detection bounds been described. Carbon (C) falls outside the detection ability of XRF but the program adopted in this study was used to calculate semi-quantitatively values for specific compounds such as Ti_3C_2. The values were normalized, as no loss of ignition (LOI) was done to determine crystal water and oxidation state changes. The presence of Al_2O_3 in significant quantity (2.4 wt. %) could be ascribed to the sample preparation [33] in the laboratory; since small amount of Al_2O_3 are expected in the parent MAX phases, also another source of Al could be the presence of some residual Al from the parent MAX phase material during the etching process to produce the Ti_3C_2. Other trace elements/compounds recorded are portrayed owing to the impurities from chemicals used in sample preparation.

3.2 Electrochemical characterization

3.2.1 Electrochemical measurements of single electrodes in a three-electrode set-up

The electrochemical evaluation of the as-synthesized electrode materials was investigated via a three-electrode measurement configuration done in 6 M KOH aqueous electrolyte. The associated CV curves of the Ti_3C_2, Mn_3O_4 and Ti_3C_2-Mn_3O_4 electrodes at 50 mV s^{-1} scan rate in both negative and positive operating potentials are

shown in Fig. 4(a-b). The different plots reveal that the Ti_3C_2-Mn_3O_4 composite electrode has a higher current response in the positive potential indicating a higher specific capacity. The CV curve of the Ti_3C_2 material compared to that of Mn_3O_4 and Ti_3C_2-Mn_3O_4 exhibits a quasi-rectangular shapes, showing a contribution of both faradic nature and electrical double layer capcitance (EDLC). The inset to Fig. 4(a) is the zoomed-in section of the CV curves of the three different materials showing clearly the overshadowed curve for the Mn_3O_4. This signifies the ability of the material to be charged and discharged at a pseudoconstant rate over the entire voltammetric cycle in the negative potential range [55].

Fig. 4 (b) displays the CV profile of the Ti_3C_2-Mn_3O_4 composite and its constituents, with that of Ni-foam pristine in the positive potential window range. It is noticed from the Fig., that the redox peaks from the Ni-foam are negligible compared to those from the as-synthesized Mn_3O_4 and Ti_3C_2-Mn_3O_4 materials which clearly depicts no contribution of capacity. An indication that the redox peaks are essentially attributed to the electrode materials.

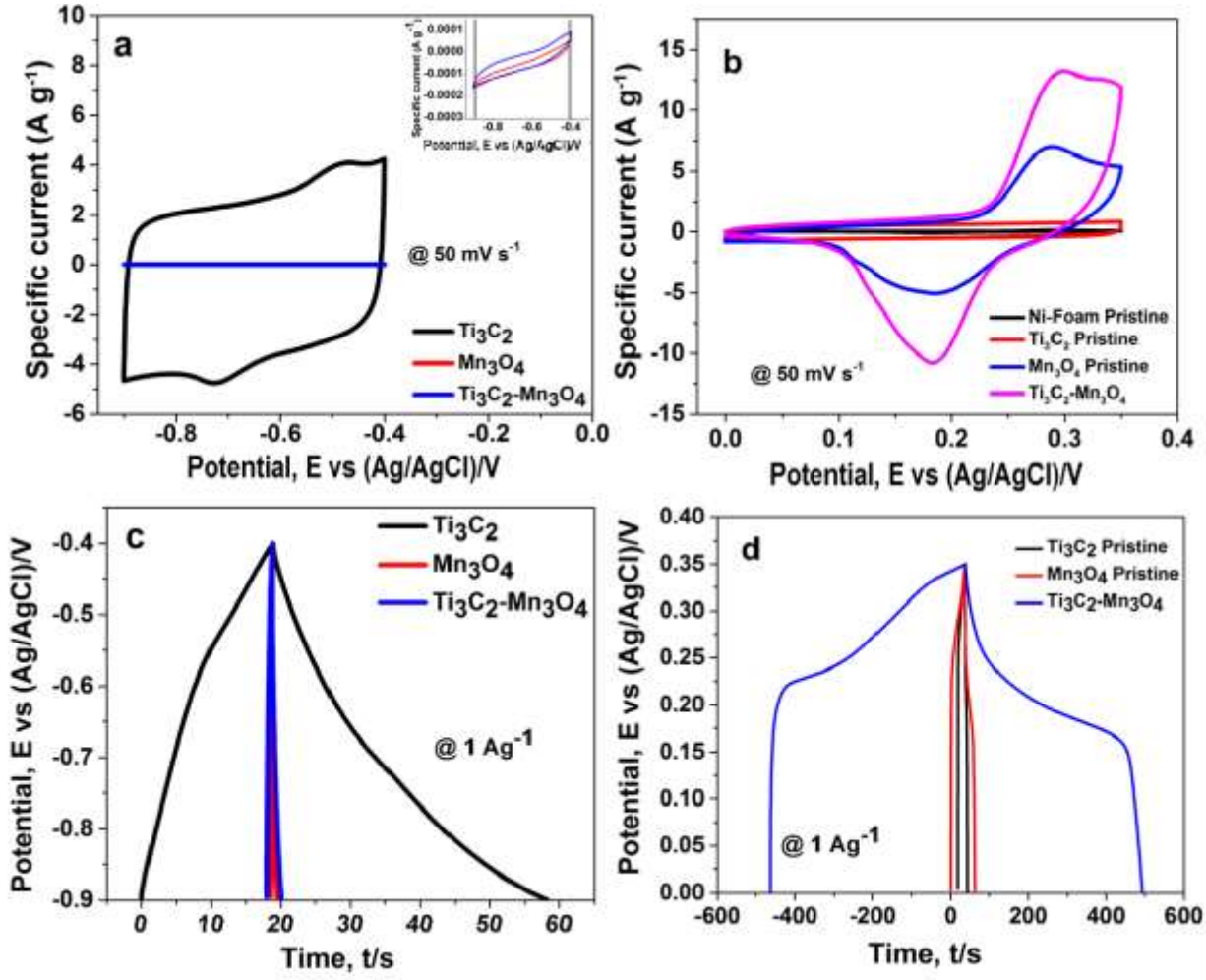

Fig. 4. CV curves of the Ti_3C_2 pristine, Mn_3O_4 pristine and Ti_3C_2-Mn_3O_4 composites (a) in the negative potential window, inset to (a) is the zoomed-in CV curves of the samples and (b) including that of pristine Ni-foam in the positive potential window at a scan rate of 50 mV s^{-1} respectively, (c) and (d) GCD curves of all the three materials in both negative and positive potentials at a specific current of 1 A g^{-1} respectively.

Additionally, the peak specific current of the Ti_3C_2-Mn_3O_4 nanocomposite is much higher than that of Ti_3C_2 and Mn_3O_4 at the same 50 mV s^{-1} scan rate implying a larger specific capacity of the material is obtainable [56]. However, it is considered that the redox peaks are essentially assigned to the Ti_3C_2-Mn_3O_4 electrode material [36].

Fig. 4 (c-d) shows a plot comparing the CD profiles of the as-synthesized electrode materials in both negative and positive potential windows indicating an improved electrochemical charge storage capability which is faraidic in nature in the positive operating potential range.

To further examine the electrochemical properties of Ti_3C_2-Mn_3O_4 nanocomposite electrode material, the CV curves at varying scan rates in a potential range of 0.0 – 0.35 V are displayed in Fig. 5 (a). The curves at distinct scanning rates show a pair of well-defined redox peaks associated with the reversible transformation of Ti^{3+}/Ti^{4+} and Mn^{3+}/Mn^{4+}.

Fig. 5 (b) shows the CD curves at different specific currents. The nonlinear CV and CD curves demonstrate oxidation and reduction peaks owing to the reversible redox faradic reaction of a mixed proportion, comprising Ti^{2+}, Ti^{3+}, Mn^{2+} and Mn^{3+} affirming the faradic property of the Ti_3C_2-Mn_3O_4 electrode. The nonlinear CD curves and the voltage plateau observed corresponds well to the peaks displayed by the CV curves [57], a further confirmation of the material's faradic behavior.

A shift of the anodic and cathodic peaks potentials in the positive and negative directions is observed with increasing scan rate (Fig. 5(a)), owing to the aggravated polarization [58,59], emanating from the inadequacy of ion diffusion rate to fulfil electronic neutralization in the redox process [60]. The redox peaks intensities are improved relative to increasing scanning rate [59]. Fig. 5 (c) displays a linear relationship of the peak specific current as a function of the square roots of scan rate. The linearity of the plots confirmed that the electrochemical reaction is diffusion controlled, and further affirms the swift faradaic charge storage process within the Ti_3C_2-Mn_3O_4 nanocomposite electrode [61].

The electrical resistance of the electrode materials was further evaluated through the EIS technique at an open circuit potential, 0.0 V with frequencies ranging from 10 mHz to100 kHz. A demonstration of the Nyquist impedance plots of the Ti_3C_2, Mn_3O_4 and Ti_3C_2-Mn_3O_4 nanocomposite is shown in Fig. 5 (d).

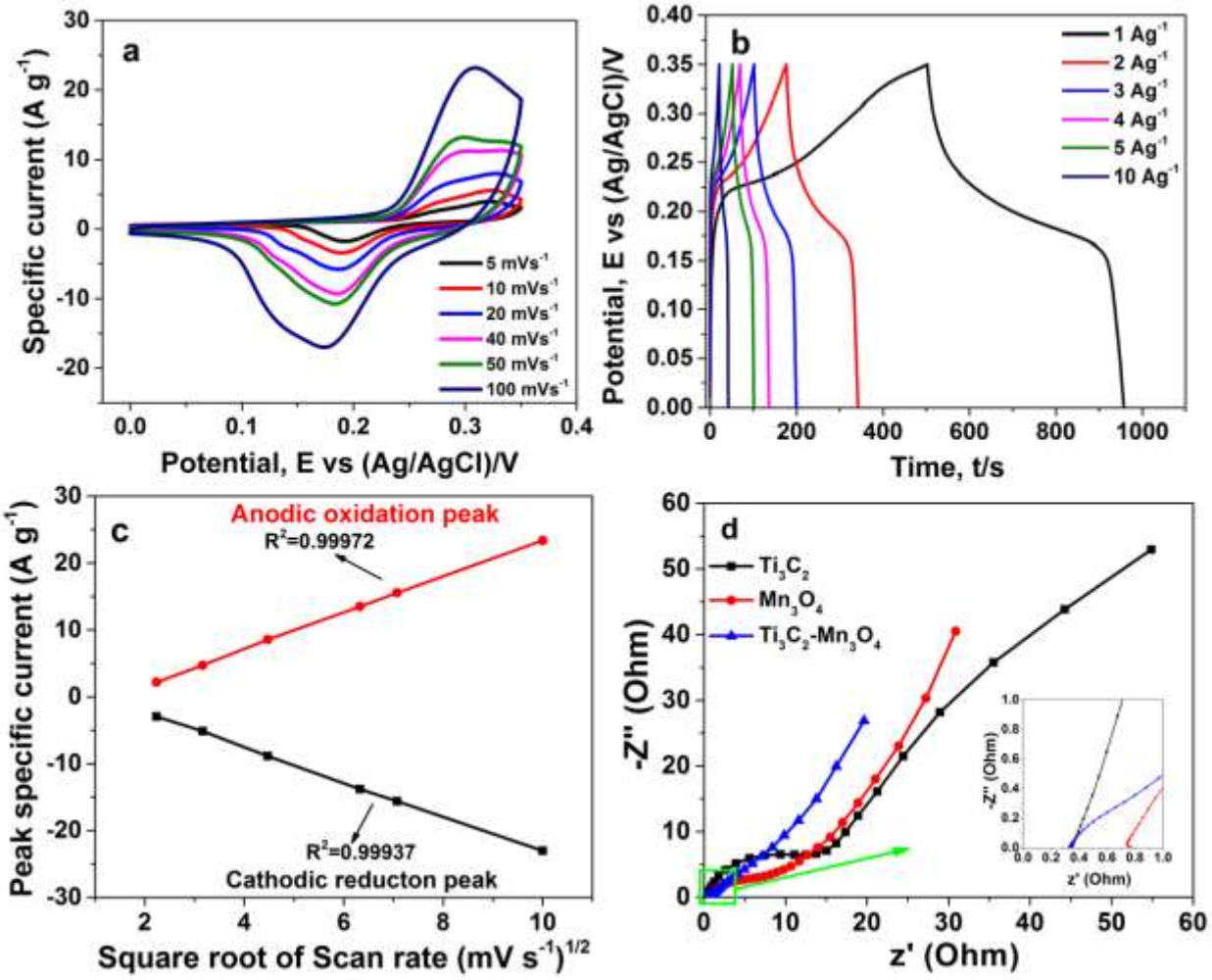

Fig. 5. (a) CV curves of the Ti_3C_2-Mn_3O_4 composite at distinct scan rates, (b) CD curves of the Ti_3C_2-Mn_3O_4 composite at various specific currents, (c) anodic and cathodic peak specific current plotted as function of square root of scan rate for Ti_3C_2-Mn_3O_4 composite and (d) EIS Niquist plots comparison of the Ti_3C_2, Mn_3O_4 and Ti_3C_2-Mn_3O_4 with an enlarged high-frequency region as the inset respectively.

From the EIS plots for all three electrodes (Fig. 5(d)), a semicircle was noticed in the high frequency region, displaying the interfacial charge transfer resistance, R_{ct} and mass transport via the material [34]. The inset to Fig. 5(d) portrays a zoomed-in high frequency region of the plots.

The intersection to the real Z' axis is attributed to the electrode series resistance, R_S that involves the electrolyte ionic resistance, the intrinsic resistance of the active materials together with the contact resistance at the electrode material/current collector interface [34].

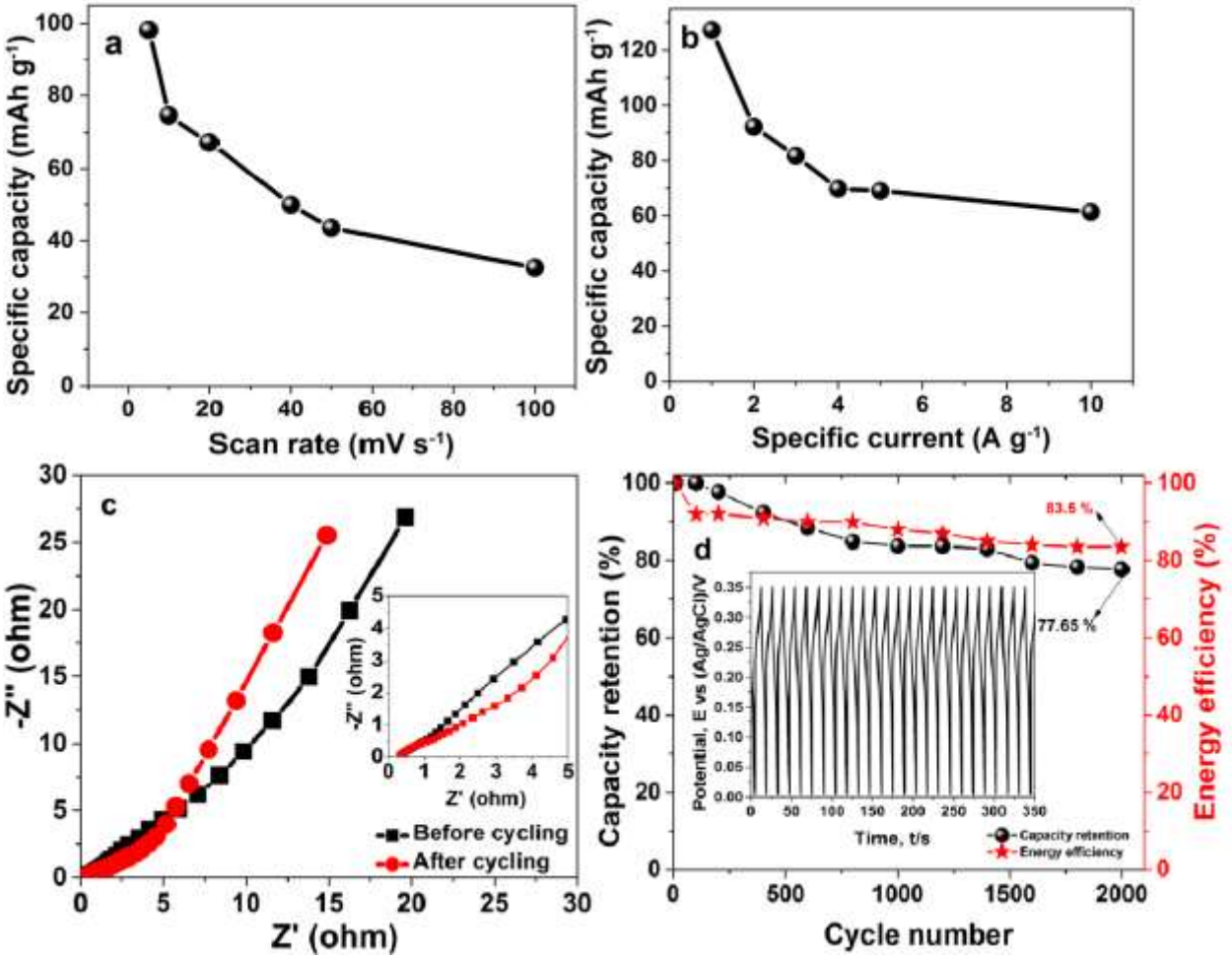

Fig. 6. Plots of (a) specific capacity vs. scan rate, and (b) specific capacity vs. specific current of the Ti_3C_2-Mn_3O_4 composite, (c) EIS Niquist plot Ti_3C_2-Mn_3O_4 composite before and after 2000 cycling, with the zoomed-in high-frequency region of the plot in the inset and (d) cycling performance of Ti_3C_2-Mn_3O_4 composite up to 2000 cycles at 10 A g^{-1}, and the corresponding few cycles of the CD profiles in the inset respectively.

From the Fig., the R_S values for the Ti_3C_2, Mn_3O_4 and Ti_3C_2-Mn_3O_4 nanocomposite electrodes were recorded as 0.35 Ω, 0.73 Ω as well as 0.31 Ω respectively. Remarkably, the low R_S of the synthesized Ti_3C_2-Mn_3O_4 electrode material implies a high electrical conductivity, resulting in a satisfying capacitive behaviour of the electrode material based on the successful integration of the metal oxide into the MXene framework.

The specific capacity values plotted against the scan rate and specific current are shown in Fig. 6 (a-b) for Ti_3C_2-Mn_3O_4 electrode material, respectively.

The obtained specific capacity values evaluated from CV profiles at increasing scan rates in a range of 5–100 mV s^{-1} was 98.2–32.6 mAh g^{-1} while the specific capacities evaluated from the curves of a more accurate CD technique at increasing specific currents of 1–10 A g^{-1} ranged from 128.0–61.5 mAh g^{-1}.

It is obvious that the material displayed a higher specific capacity (128 mAh g^{-1}) compared to some other similar Ti_3C_2, and Mn_3O_4-based composites materials earlier reported in the literature [1,38,43,46,58-63]. The high performance is ascribed to the presence of an optimized orientation of the MXene material in combination with the metal oxide material which synergistically improved the individual properties of both material to provide a combined improved conductivity, swift electron transportation, and larger SSA for more access to aqueous electrolyte to the electrodes [51].

The higher specific capacity values could be attributed to the introduction of Mn_3O_4 nanoparticles, which further modifies the morphology and structure of the Ti_3C_2-Mn_3O_4 nanocomposite sample. Besides, Mn_3O_4 nanoparticles may act like a template for mitigating potential volume changes from cations insertion, and as well as a secondary current collector providing supports for electronic conductivity in the composite reflecting the massive charge being stocked everywhere in the material as well as at the electrolyte-electrode interface compared to Ti_3C_2 electrode [36,64]. Also, the Ti_3C_2 nanosheets in the composite sample perform as conductive span as well as nanoscale collector for electron transfer [1,39].

Fig. 6 (c) demonstrates the EIS graphs of Ti_3C_2-Mn_3O_4 electrode before, and over 2000 charge and discharge cycling at 10 A g^{-1}. The semicircle in the high frequency region

shows that resistance of the composite electrode material slightly increased after 2000 cycles as indicated by the inset to Fig. 6 (c).

Fig. 6 (d) is the specific capacity retention and energy efficiency of the Ti_3C_2-Mn_3O_4 composite electrode plotted the cycle number. A discharge capacity of about 77.7% was retained for the single electrode, with a corresponding energy efficiency of about 83.5% for over 2000 cycles at 10 A g^{-1}. The high capacity retention could be ascribed to the material's higher electronic conductivity and the particular pore and perfect separated layered nanosheets structure of Ti_3C_2-Mn_3O_4 material. Moreover, the Ti_3C_2 nanosheets in Ti_3C_2-Mn_3O_4 nanocomposite electrode supply good adhesion to the Mn_3O_4 nanomaterial with a π-π bonding energy which keeps the material intact. This bonding helps to stabilize the Ti_3C_2-Mn_3O_4 nanocomposite mechanically, preventing loss of electrode material while cycling against the prevalent trend of dissolution of Manganese into the electrolyte solution and improves the cycle life of Mn_3O_4-based material electrodes [65,66].

3.2.2. Electrochemical evaluations of the hybrid Ti_3C_2-Mn_3O_4//C-FP supercapattery

Owing to the remarkable performance of Ti_3C_2-Mn_3O_4 nanocomposite electrode material, a hybrid supercapattery was assembled and named as Ti_3C_2-Mn_3O_4//C-FP, with Ti_3C_2-Mn_3O_4: C-FP mass balancing ratio, evaluated using equation 7, as 1.00: 0.74 corresponding to an aerial mass loading of approximately 1.9 and 1.47 mg/cm^2 with an electrode area of nearly 1.54 cm^2, resulting in a mass of ~ 2.9 and 2.3 mg for Ti_3C_2-Mn_3O_4 and C-FP chosen as positive and negative electrodes, accordingly, and a total mass of ~ 5.2 mg (~ 3.37 mg/cm^2) for both Ti_3C_2-Mn_3O_4 and C-FP active materials components in the hybrid asymmetric device.

Fig. 7 (a) indicates the CV curves of Ti_3C_2-Mn_3O_4 and C-FP tested as single electrodes at a scan rate of 20 mV s^{-1}. The C-FP material electrode displayed a quasi-rectangular CV curve that is truly comparable to double-layer capacitive properties. The assembled hybrid device as observed in Fig. 7 (c), could operate in a much larger potential window up to 1.5 V. Fig. 7 (b) depicts the potential profiles of Ti_3C_2-Mn_3O_4 and C-FP, at a specific current of 1 A g^{-1}. The C-FP negative electrode delivers a specific capacitance of 235 F g^{-1} at 1 A g^{-1} within -1.2 V to 0 V potential ranges. Fig. 7 (c) displays the CV curves of the hybrid Ti_3C_2-Mn_3O_4//C-FP device performed at distinct scan rates in the range of 5 to 100 mV s^{-1}. To our notice, the CV profiles at distinct scan rates portrays a mix of faradic and that of electric-double layer capacitive behaviors, a characteristic feature associated with hybrid SCs [34,67]. Fig. 7 (d) exhibits the CD profiles of the assembled device at various specific currents. The non-symmetric CD profiles indicates the faradaic contribution via redox reactions to the hybrid Ti_3C_2-Mn_3O_4//C-FP device [34,67,68]. This also confirms the assertion made earlier regarding the results from the CV plots demonstrated in Fig. 7 (c). The nonlinear variation between potential and time indicates a typical of faradaic process, which is as a result of the electrochemical redox reactions in the material components of the device. The similarly nonlinear CD profiles observed for the device implies that the capacity mostly results from the faradaic/redox reactions. This indication matched well with the results observed from the CV curves in Fig. 7 (c). The observed asymmetry in the CD curves below the ~ 1.2V potential is attributed to some incompletely reversible electrochemical redox reaction [69].

Fig. 8 (a) demonstrates the estimated specific capacities of the Ti_3C_2-Mn_3O_4//C-FP device using equation 2 and plotted against different specific currents. At specific current of 1 A g^{-1}, the device was noticed to produce maximum a specific capacity of 78.9 mA h g^{-1}.

Fig. 8 (b) is a display of the Ragone chart of energy and power densities as two key parameters used to ascertain the applicability of a device. The equivalent energy density together with power density of the assembled device were calculated using equations 4 and 5. A high energy density of 28.3 Wh kg^{-1}, equivalent to a power density of 463.4 W kg^{-1} at a specific current of 1 A g^{-1} was recorded. Remarkably, the device retained a notably high energy density of 22.2 Wh kg^{-1} that is equal to a power density of 2285.5 W kg^{-1} at 5 A g^{-1} specific current.

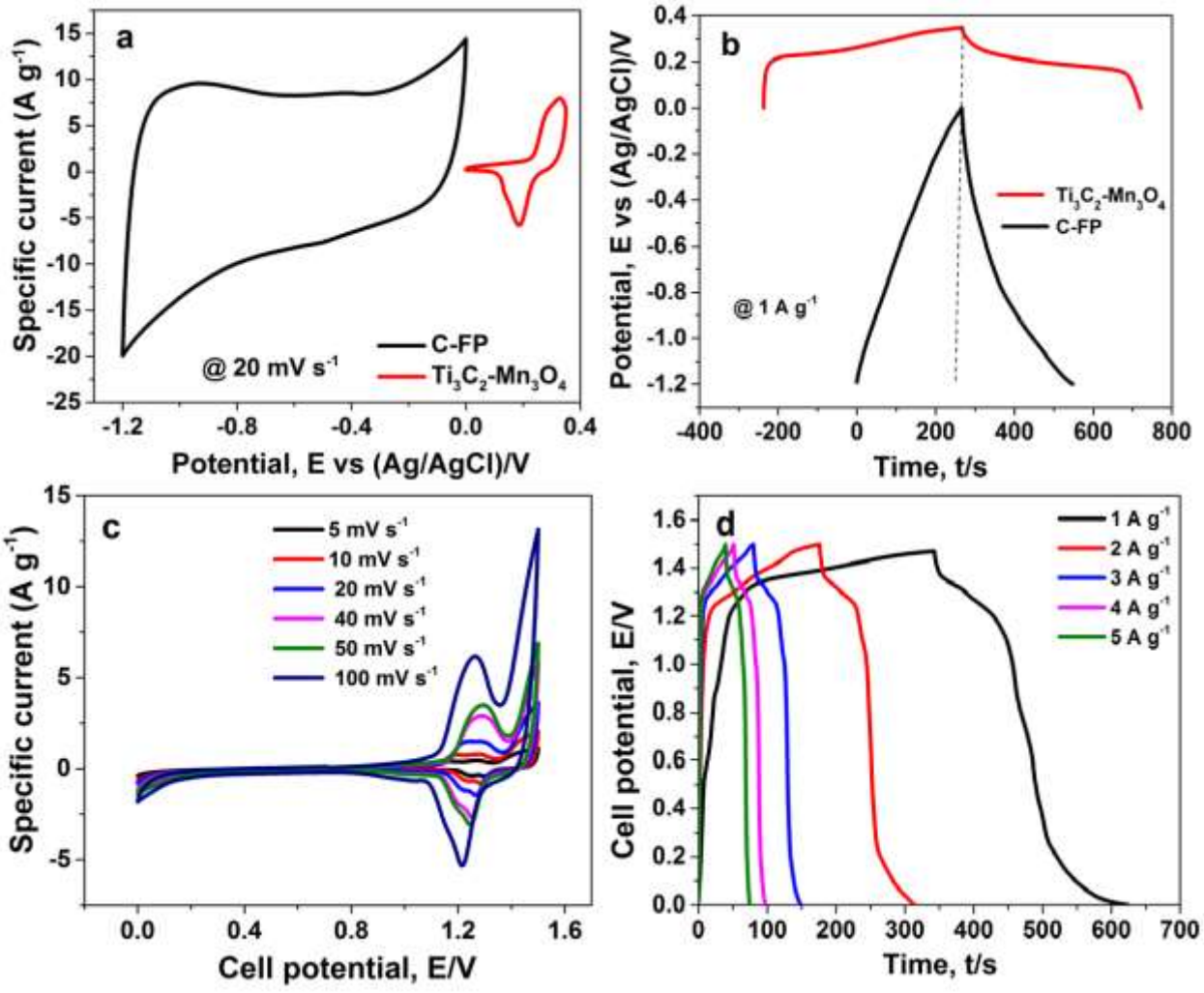

Fig. 7. (a) CV curves of Ti_3C_2-Mn_3O_4 and C-FP, (b) CD curves of Ti_3C_2-Mn_3O_4 and C-FP, (c) CV curves of Ti_3C_2-Mn_3O_4//C-FP at distinct scan rates, and (d) CD profiles of Ti_3C_2-Mn_3O_4//C-FP at various specific currents of the asymmetric device.

This is an indication that the assembled hybrid *SC* is able to deliver a large power density without a significant loss of the stored energy [34]. This indication resolves the importance of the point that as greatly as the hope in the study of supercapacitor is to enhance its energy capability to contend with that of battery, but not expected to be accomplished at the cost of compromising its power density [34]. The energy density obtained for asymmetric device in this work compares well with some other recently published asymmetric devices in the literature [70–73].

From Fig. 8 (c), it could be noticed that the device showcased a superior energy efficiency of 90.2 % determined using equation 3. The device also preserved 92.6 % of the initial capacity after continuously cycling for up to a 10000 cycles at a specific current of 3 A g^{-1}. This demonstrates an excellent long-term electrochemical stability of the asymmetric device. Such remarkable stability is mostly uncommon for supercapattery-type devices but EDLC. The unmatched behavior is ascribed to the mesoporous nature of the Ti_3C_2-Mn_3O_4 nanocomposite material that plays a crucial part in raising the efficient electrode surface area, easing electrolyte permeability, thereby narrowing electron pathway in the active materials [34,73]. The mesopores in the Ti_3C_2-Mn_3O_4 nanocomposite structure provide improved accessibility towards the reactant molecules cations through the interlayer space [75]. Furthermore, the distinguished mesoporous structure could suit well the OH^- ions, thus promoting electrochemical improvement as a result of closely packed ionic layers lying on both adjoining hole walls [74,76]. This mesoporous nature could as well contribute to ion and electron flow, repressing any modification of electrode volume in the charge-discharge process [77].

In Fig. 8(d) the EIS analysis employed to further assess the properties of the device is shown. From the plots, the solution resistances, R_s before and after 10000 cycles were estimated to be 0.86 Ω and 0.89 Ω, respectively, showing the suitability of electrical

behaviours of the material adopted in fabricating the hybrid *SC*. The R_s which occurs at the intercept to the Z'-axis in the high frequency region, is a summed up of resistance in the electrolyte together with that between the contact and the material electrode.

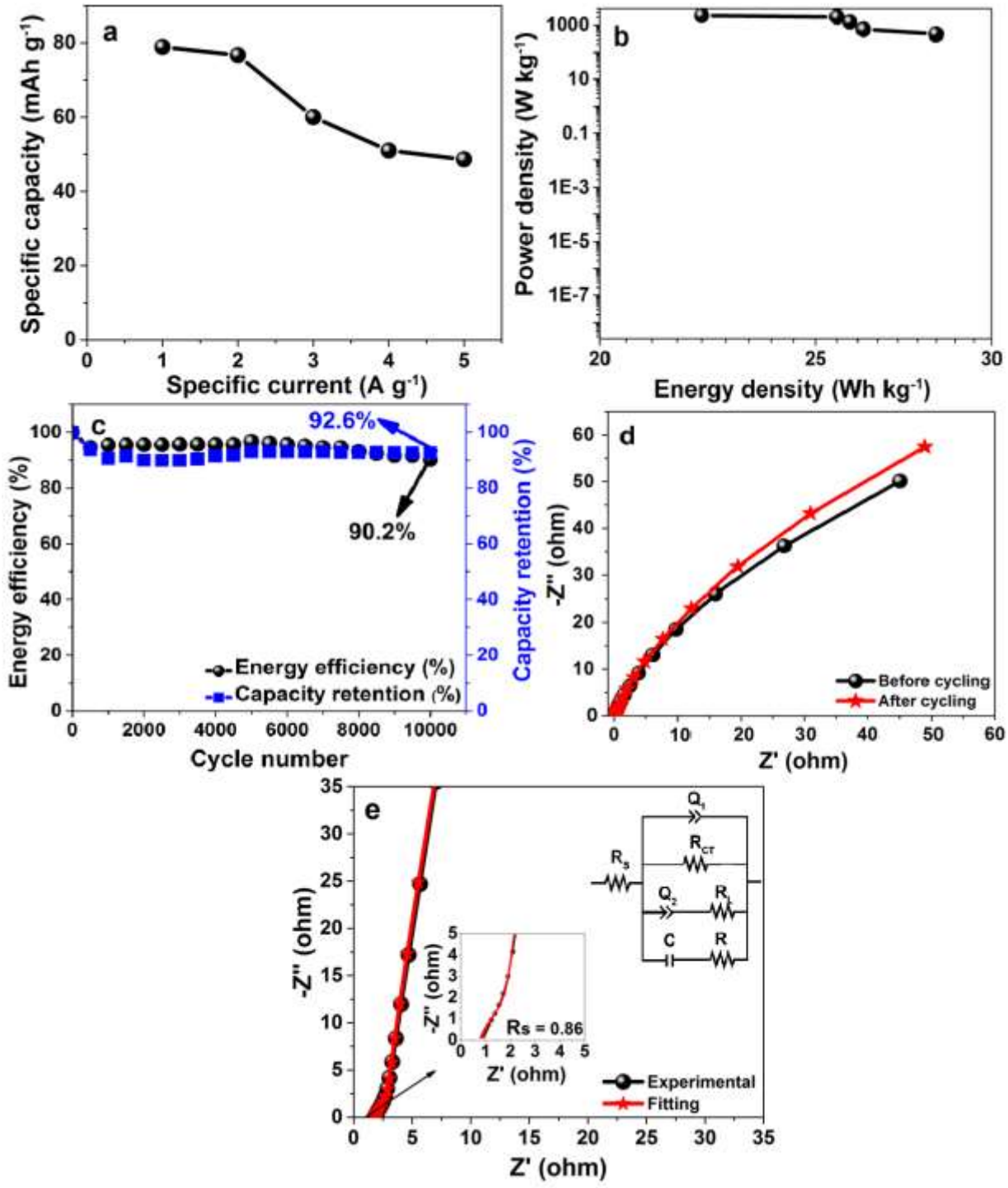

Fig. 8. (a) Specific capacity vs. specific current and (b) Ragone plot, (c) cyclic performance, (d) EIS before and over 10000 cycles at a specific current of 3 A g^{-1}, and (e) the fitted Nyquist plot by using equivalent circuit (inset) of the Ti_3C_2-Mn_3O_4//C-FP asymmetric device.

Following cycling, the diffusion path length was noticed to have drifted towards the optimal perpendicular nature, and is attributed to the optimum use or sufficient active material during redox reaction [34], irrespective of the high specific current.

Moreover, the Nyquist plot for Ti_3C_2-Mn_3O_4//C-FP asymmetric device was fitted as shown in Fig. 8(e) with aid of a ZFIT fitting program v11.02, with its corresponding electrical circuit displayed in the inset. From the circuit, the R_S is joined in series with a constant phase element (CPE) Q_1, that is parallely connected to the charge transfer resistance, R_{CT}. The leakage current resistance, R_L is in series with another CPE, Q_2. The mass capacitance indicated as C is joined parallel to load resistance, R_L, all of which are in series with the R_S.

Conclusion

Ti_3C_2-Mn_3O_4 nanocomposite electrode materials were successfully synthesized by a solvothermal process which permits for the exact influence on the magnitude, form, as well as crystallinity of the metal oxide nanostructures, by introducing Mn_3O_4 into the Ti_3C_2 layers with the aim of taking advantage of the surface functionalities on the MXene sheets. The characterization of the composite electrode material confirmed that the as-synthesized material is composed of a layered structure of nanosheets which are clearly delaminated with the integration of the metal oxide nanoparticles into the interlayer spaces. The material demonstrated an enhanced electrochemical performance with a recorded specific capacity value of 128 mAh g^{-1} at specific current of 1 A g^{-1}. A great performance was illustrated by the Ti_3C_2-Mn_3O_4 composite material capacity, satisfactory cycling stability as well as the 77.65 % capacity retention ability for up to 2000 constant CD cycles at 10 A g^{-1}. An assembled low cost hybrid Ti_3C_2-

Mn_3O_4//C-FP SC device in 6 M KOH electrolyte yielded a comparable energy density of 28.32 Wh kg^{-1} with an equivalent high power density of 463.42 W kg^{-1} at a specific current of 1 A g^{-1}, and a 92.6% capacity retention for over 10000 cycling test. The device was observed to maintain a considerably high energy density of 22.22 Wh kg^{-1} with corresponding power density of 2285.49 W kg^{-1} at a high specific current of 5 A g^{-1}. The research provides an addition to the knowledge of 2D MXene-based composites and is useful in designing novel high-performance hybrid electrode materials with promising device efficiency for supercapacitors applications.

Acknowledgements

This study is supported by the South African Research Chairs Initiative of the Department of Science and Technology and National Research Foundation of South Africa (Grant No. 61056). All observations and results put forward in this material are those of the authors, and the NRF does not take a liability regarding this. The authors are grateful for the invaluable inputs by Prof. Yury Gogotsi of the Department of Materials Science & Engineering, Drexel University, 3141 Chestnut Street, Philadelphia 19104, USA. Dr. Farshad Barzegar of the University of Pretoria is acknowledged for valuable discussions. K. O. appreciates the financial assistance from the University of Pretoria and National Research Foundation (NRF) for studentship grants.

References

[1] C. Zhao, Q. Wang, H. Zhang, S. Passerini, X. Qian, Two-Dimensional Titanium Carbide/RGO Composite for High-Performance Supercapacitors, ACS Appl. Mater. Interfaces. 8 (2016) 15661–15667. doi:10.1021/acsami.6b04767.

[2] G. Yu, X. Xie, L. Pan, Z. Bao, Y. Cui, Hybrid nanostructured materials for high-performance electrochemical capacitors, Nano Energy. 2 (2013) 213–234. doi:10.1016/j.nanoen.2012.10.006.

[3] F. Wang, M. Cao, Y. Qin, J. Zhu, L. Wang, Y. Tang, ZnO nanoparticle-decorated two-dimensional titanium carbide with enhanced supercapacitive performance, RSC Adv. 6 (2016) 88934–88942. doi:10.1039/C6RA15384D.

[4] P. Liu, M. Verbrugge, S. Soukiazian, Influence of temperature and electrolyte on the performance of activated-carbon supercapacitors, J. Power Sources. 156 (2006) 712–718. doi:10.1016/j.jpowsour.2005.05.055.

[5] Z. Zhang, Q. Wang, C. Zhao, S. Min, X. Qian, One-Step Hydrothermal Synthesis of 3D Petal-like Co 9 S 8 /RGO/Ni 3 S 2 Composite on Nickel Foam for High-Performance Supercapacitors, *ACS applied materials & interfaces*, *7* (2015), 4861-4868. doi:10.1021/am5088192.

[6] K.S. Novoselov, A.K. Geim, S. V. Morozov, D. Jiang, Y. Zhang, S. V. Dubonos, I. V. Grigorieva, A.A. Firsov, Electric Field Effect in Atomically Thin Carbon Films, Science, 306 (2004) 666-669. doi: 10.1126/science.1102896.

[7] H. Zhang, Ultrathin Two-Dimensional Nanomaterials, ACS Nano Lecturesh. Award. 9 (2015) 9451–9469. doi:10.1021/acsnano.5b05040.

[8] Y. Liu, X. Peng, Recent advances of supercapacitors based on two-dimensional materials, Appl. Mater. Today. 7 (2017) 1–12. doi:10.1016/j.apmt.2017.01.004.

[9] T. Palaniselvam, J.-B. Baek, Graphene based 2D-materials for supercapacitors, 2D Mater. 2 (2015) 032002. doi:10.1088/2053-1583/2/3/032002.

[10] X. Peng, L. Peng, C. Wu, Y. Xie, Two dimensional nanomaterials for flexible supercapacitors, Chem. Soc. Rev. 43 (2014) 3303. doi:10.1039/c3cs60407a.

[11] M. Naguib, V.N. Mochalin, M.W. Barsoum, Y. Gogotsi, 25th anniversary article: MXenes: A new family of two-dimensional materials, Adv. Mater. 26 (2014) 992–1005. doi:10.1002/adma.201304138.

[12] L. Dong, H. Kumar, B. Anasori, Y. Gogotsi, V.B. Shenoy, Rational Design of Two-Dimensional Metallic and Semiconducting Spintronic Materials Based on Ordered Double-Transition-Metal MXenes, J. Phys. Chem. Lett. 8 (2017). doi:10.1021/acs.jpclett.6b02751.

[13] B. Anasori, M.R. Lukatskaya, Y. Gogotsi, 2D metal carbides and nitrides (MXenes) for energy storage, Nat. Rev. Mater. 2 (2017) 16098. doi:10.1038/natrevmats.2016.98.

[14] A.D. Dillon, M.J. Ghidiu, A.L. Krick, J. Griggs, S.J. May, Y. Gogotsi, M.W. Barsoum, A.T. Fafarman, Highly Conductive Optical Quality Solution-Processed Films of 2D Titanium Carbide, Adv. Funct. Mater. 26 (2016) 4162–4168. doi:10.1002/adfm.201600357.

[15] X. Liang, A. Garsuch, L.F. Nazar, Sulfur Cathodes Based on Conductive MXene Nanosheets for High-Performance Lithium-Sulfur Batteries, Angew. Chemie Int. Ed. 54 (2015) 3907–3911. doi:10.1002/anie.201410174.

[16] C.E. Ren, K.B. Hatzell, M. Alhabeb, Z. Ling, K.A. Mahmoud, Y. Gogotsi, Charge- and Size-Selective Ion Sieving Through $Ti_3C_2T_x$ MXene Membranes, J. Phys. Chem. Lett. 6 (2015) 4026–4031. doi:10.1021/acs.jpclett.5b01895.

[17] Z.W. Seh, K.D. Fredrickson, B. Anasori, J. Kibsgaard, A.L. Strickler, M.R. Lukatskaya, Y. Gogotsi, T.F. Jaramillo, A. Vojvodic, Two-Dimensional Molybdenum Carbide (MXene) as an Efficient Electrocatalyst for Hydrogen Evolution, ACS Energy Lett. 1 (2016) 589–594. doi:10.1021/acsenergylett.6b00247.

[18] F. Shahzad, M. Alhabeb, C.B. Hatter, B. Anasori, S. Man Hong, C.M. Koo, Y. Gogotsi, Electromagnetic interference shielding with 2D transition metal carbides (MXenes), Science, 353 (2016) 1137-1140. doi: 10.1126/science.aag2421.

[19] M. Naguib, J. Halim, J. Lu, K.M. Cook, L. Hultman, Y. Gogotsi, M.W. Barsoum, New two-dimensional niobium and vanadium carbides as promising materials for li-ion batteries, J. Am. Chem. Soc. 135 (2013) 15966-15969. doi:10.1021/ja405735d.

[20] C. Eames, M.S. Islam, Ion intercalation into two-dimensional transition-metal carbides: Global screening for new high-capacity battery materials, J. Am. Chem. Soc. 136 (2014) 16270-16276. doi:10.1021/ja508154e.

[21] M. Naguib, O. Mashtalir, J. Carle, V. Presser, J. Lu, L. Hultman, Y. Gogotsi, M.W. Barsoum, Two-Dimensional Transition Metal Carbides Herein we report on the synthesis of two-dimensional transition metal carbides, *ACS nano.* 6 (2012) 1322-1331. doi:10.1021/nn204153h.

[22] J. Pike, J. Hanson, L. Zhang, S. Chan, Synthesis and Redox Behavior of Nanocrystalline Hausmannite (Mn_3O_4), Chem. Mater. 19 (2007) 5609–5616. doi:10.1021/cm071704b.

[23] J.C. Nardi, Characterization of the LiMnO[sub 2] Multistep Discharge, J. Electrochem. Soc. 132 (1985) 1787. doi:10.1149/1.2114218.

[24] X. Li, L. Zhou, J. Gao, H. Miao, H. Zhang, J. Xu, Synthesis of Mn_3O_4 nanoparticles and their catalytic applications in hydrocarbon oxidation, Powder Technol. 190 (2009) 324–326. doi:10.1016/j.powtec.2008.08.010.

[25] C.J. Jafta, F. Nkosi, L. le Roux, M.K. Mathe, M. Kebede, K. Makgopa, Y. Song, D. Tong, M. Oyama, N. Manyala, S. Chen, K.I. Ozoemena, Manganese oxide/graphene oxide composites for high-energy aqueous asymmetric electrochemical capacitors, Electrochim. Acta. 110 (2013) 228–233. doi:10.1016/j.electacta.2013.06.096.

[26] K. Makgopa, P.M. Ejikeme, C.J. Jafta, K. Raju, M. Zeiger, V. Presser, K.I. Ozoemena, A high-rate aqueous symmetric pseudocapacitor based on highly graphitized onion-like carbon/birnessite-type manganese oxide nanohybrids, J. Mater. Chem. A. 3 (2015) 3480–3490. doi:10.1039/C4TA06715K.

[27] A. Bello, O.O. Fashedemi, J.N. Lekitima, M. Fabiane, D. Dodoo-Arhin, K.I. Ozoemena, Y. Gogotsi, A.T. Charlie Johnson, N. Manyala, High-performance symmetric electrochemical capacitor based on graphene foam and nanostructured manganese oxide, AIP Adv. 3 (2013) 082118. doi:10.1063/1.4819270.

[28] Y. Hu, J. Chen, X. Xue, T. Li, Synthesis of monodispersed single-crystal

compass-shaped Mn_3O_4 via gamma-ray irradiation, Mater. Lett. 60 (2006) 383–385. doi:10.1016/j.matlet.2005.08.056.

[29] K.I. Ozoemena, K. Raju, P.M. Ejikeme, K.I. Ozoemena, High-performance Mn3O4/onion-like carbon (OLC) nanohybrid pseudocapacitor: Unravelling the intrinsic properties of OLC against other carbon supports, Carbon N. Y. 117 (2017) 20–32. doi:10.1016/j.carbon.2017.02.050.

[30] T. Xiong, W.S.V. Lee, X. Huang, J.M. Xue, Mn_3O_4 /reduced graphene oxide based supercapacitor with ultra-long cycling performance, J. Mater. Chem. A. 5 (2017) 12762–12768. doi:10.1039/C7TA03319B.

[31] C.-L. Liu, K.-H. Chang, C.-C. Hu, W.-C. Wen, Microwave-assisted hydrothermal synthesis of Mn_3O_4/reduced graphene oxide composites for high power supercapacitors, J. Power Sources. 217 (2012) 184–192. doi:10.1016/j.jpowsour.2012.05.109.

[32] Q. Jiangying, G. Feng, Z. Quan, W. Zhiyu, H. Han, L. Beibei, W. Wubo, W. Xuzhen, Q. Jieshan, Highly atom-economic synthesis of graphene/Mn_3O_4 hybrid composites for electrochemical supercapacitors, Nanoscale. 5 (2013) 2999. doi:10.1039/c3nr33700f.

[33] M. Naguib, M. Kurtoglu, V. Presser, J. Lu, J. Niu, M. Heon, L. Hultman, Y. Gogotsi, M.W. Barsoum, Two-dimensional nanocrystals produced by exfoliation of Ti_3AlC_2, Adv. Mater. 23 (2011) 4248–4253. doi:10.1002/adma.201102306.

[34] K.O. Oyedotun, M.J. Madito, D.Y. Momodu, A.A. Mirghni, T.M. Masikhwa, N. Manyala, Synthesis of ternary NiCo-MnO_2 nanocomposite and its application as a novel high energy supercapattery device, Chem. Eng. J. 335 (2018) 416–433. doi:10.1016/j.cej.2017.10.169.

[35] M.N. Rantho, M.J. Madito, F.O. Ochai-Ejeh, N. Manyala, an Asymmetric supercapacitor based on vanadium disulfide nanosheets as a cathode and carbonized iron cations adsorbed onto polyaniline as node, Electrochim. Acta. 260 (2017) 11–23. doi:10.1016/j.electacta.2017.11.074.

[36] K.O. Oyedotun, M.J. Madito, A. Bello, D.Y. Momodu, A.A. Mirghni, N. Manyala, Investigation of graphene oxide nanogel and carbon nanorods as electrode for electrochemical supercapacitor, Electrochim. Acta. 245 (2017) 268–278. doi:10.1016/j.electacta.2017.05.150.

[37] R.B. Rakhi, B. Ahmed, M.N. Hedhili, D.H. Anjum, H.N. Alshareef, Effect of post-etch annealing gas composition on the structural and electrochemical properties of Ti2CTx MXene electrodes for supercapacitor applications, Chem. Mater. 27 (2015) 5314-5323. doi:10.1021/acs.chemmater.5b01623.

[38] F. Davar, M. Salavati-Niasari, N. Mir, K. Saberyan, M. Monemzadeh, E. Ahmadi, Thermal decomposition route for synthesis of Mn3O4 nanoparticles in presence of a novel precursor, Polyhedron. 29 (2010) 1747–1753. doi:10.1016/j.poly.2010.02.026.

[39] K. Wang, C. Zhao, S. Min, X. Qian, Facile synthesis of Cu_2O/RGO/$Ni(OH)_2$ nanocomposite and its double synergistic effect on supercapacitor performance,

Electrochim. Acta. 165 (2015) 314-322. doi:10.1016/j.electacta.2015.03.029.

[40] M. Ghidiu, J. Halim, S. Kota, D. Bish, Y. Gogotsi, M.W. Barsoum, Ion-Exchange and Cation Solvation Reactions in Ti_3C_2 MXene, Chem. Mater. 28 (2016) 3507–3514. doi:10.1021/acs.chemmater.6b01275.

[41] Y. Li, X. Zhou, J. Wang, Q. Deng, M. Li, S. Du, Y.-H. Han, J. Lee, Q. Huang, Facile preparation of in situ coated $Ti_3C_2T_x$ /$Ni_{0.5}$ $Zn_{0.5}$ Fe_2 O_4 composites and their electromagnetic performance, RSC Adv. 7 (2017) 24698–24708. doi:10.1039/C7RA03402D.

[42] M. Naguib, O. Mashtalir, M.R. Lukatskaya, B. Dyatkin, C. Zhang, V. Presser, Y. Gogotsi, M.W. Barsoum, One-step synthesis of nanocrystalline transition metal oxides on thin sheets of disordered graphitic carbon by oxidation of MXenes, Chem. Commun. 50 (2014) 7420–7423. doi:10.1039/C4CC01646G.

[43] J. Zhu, Y. Tang, C. Yang, F. Wang, M. Cao, Composites of TiO_2 Nanoparticles Deposited on Ti_3C_2 MXene Nanosheets with Enhanced Electrochemical Performance, J. Electrochem. Soc. 163 (2016) A785–A791. doi:10.1149/2.0981605jes.

[44] A.A. Khaleed, A. Bello, J.K. Dangbegnon, M.J. Madito, O. Olaniyan, F. Barzegar, K. Makgopa, K.O. Oyedotun, B.W. Mwakikunga, S.C. Ray, N. Manyala, Solvothermal synthesis of surfactant free spherical nickel hydroxide/graphene oxide composite for supercapacitor application, J. Alloys Compd. 721 (2017) 80–91. doi.org/10.1016/j.jallcom.2017.05.310.

[45] Y. Liu, R. Wang, X. Yan, Synergistic Effect between Ultra-Small Nickel Hydroxide Nanoparticles and Reduced Graphene Oxide sheets for the Application in High-Performance Asymmetric Supercapacitor, Sci. Rep. 5 (2015) 11095. doi:10.1038/srep11095.

[46] M. Naguib, T. Saito, S. Lai, M.S. Rager, T. Aytug, M. Parans Paranthaman, M.-Q. Zhao, Y. Gogotsi, $Ti_3C_2T_x$ (MXene)–polyacrylamide nanocomposite films, RSC Adv. 6 (2016) 72069–72073. doi:10.1039/C6RA10384G.

[47] C. Zhang, M. Beidaghi, M. Naguib, M.R. Lukatskaya, M.Q. Zhao, B. Dyatkin, K.M. Cook, S.J. Kim, B. Eng, X. Xiao, D. Long, W. Qiao, B. Dunn, Y. Gogotsi, Synthesis and Charge Storage Properties of Hierarchical Niobium Pentoxide/Carbon/Niobium Carbide (MXene) Hybrid Materials, Chem. Mater. 28 (2016) 3937–3943. doi:10.1021/acs.chemmater.6b01244.

[48] Y. Tang, J. Zhu, C. Yang, F. Wang, Enhanced supercapacitive performance of manganese oxides doped two-dimensional titanium carbide nanocomposite in alkaline electrolyte, J. Alloys Compd. 685 (2016) 194–201. doi:10.1016/j.jallcom.2016.05.221.

[49] Y. Qiao, Q. Sun, H. Cui, D. Wang, F. Yang, X. Wang, Synthesis of micro/nano-structured Mn_3O_4 for supercapacitor electrode with excellent rate performance, RSC Adv. 5 (2015) 31942–31946. doi:10.1039/c5ra02395e.

[50] J. Xiang, Y. Ding, L. Du, J. Li, Growth mechanism of atomic-layer-deposited TiAlC metal gate based on $TiCl_4$ and TMA precursors, Chinese Phys. B. 25 (2016) 1–4.

doi:10.1088/1674-1056/25/3/037308.

[51] Y. Tang, J. Zhu, C. Yang, F. Wang, Enhanced Capacitive Performance Based on Diverse Layered Structure of Two-Dimensional Ti_3C_2 MXene with Long Etching Time, J. Electrochem. Soc. 163 (2016) A1975–A1982. doi:10.1149/2.0921609jes.

[52] J. Duan, S. Chen, S. Dai, S.Z. Qiao, Shape control of Mn_3O_4 nanoparticles on nitrogen-doped graphene for enhanced oxygen reduction activity, Adv. Funct. Mater. 24 (2014) 2072–2078. doi:10.1002/adfm.201302940.

[53] F. Zheng, D. Zhu, X. Shi, Q. Chen, Metal–organic framework-derived porous $Mn_{1.8}$ $Fe_{1.2}$ O_4 nanocubes with an interconnected channel structure as high-performance anodes for lithium ion batteries, J. Mater. Chem. A. 3 (2015) 2815–2824. doi:10.1039/C4TA06150K.

[54] C. Yuan, J. Li, L. Hou, X. Zhang, L. Shen, X.W. Lou, Ultrathin mesoporous $NiCo_2O_4$ nanosheets supported on Ni foam as advanced electrodes for supercapacitors, Adv. Funct. Mater. 22 (2012) 4592–4597. doi:10.1002/adfm.201200994.

[55] M.R. Lukatskaya, S.-M. Bak, X. Yu, X.-Q. Yang, M.W. Barsoum, Y. Gogotsi, Probing the Mechanism of High Capacitance in 2D Titanium Carbide Using In Situ X-Ray Absorption Spectroscopy, Adv. Energy Mater. 5 (2015) 1500589. doi:10.1002/aenm.201500589.

[56] M. Li, J.P. Cheng, J.H. Fang, Y. Yang, F. Liu, X.B. Zhang, NiAl-layered Double Hydroxide/Reduced Graphene Oxide Composite: Microwave-assisted Synthesis and Supercapacitive Properties, Electrochim. Acta. 134 (2014) 309–318. doi:10.1016/j.electacta.2014.04.141.

[57] X. Xiao, B. Han, G. Chen, L. Wang, Y. Wang, Preparation and electrochemical performances of carbon sphere@ZnO core-shell nanocomposites for supercapacitor applications, Sci. Rep. 7 (2017) 40167. doi:10.1038/srep40167.

[58] J. Li, X. Cao, A. Pan, Y. Zhao, H. Yang, G. Cao, S. Liang, Nanoflake-assembled three-dimensional $Na_3V_2(PO_4)_3$/C cathode for high performance sodium ion batteries, Chem. Eng. J. 335 (2018) 301–308. doi:10.1016/j.cej.2017.10.164.

[59] X. Cao, A. Pan, Y. Zhang, J. Li, Z. Luo, X. Yang, S. Liang, G. Cao, Nanorod-Nanoflake Interconnected $LiMnPO_4 \cdot Li_3V_2(PO_4)_3$/C Composite for High-Rate and Long-Life Lithium-Ion Batteries, ACS Appl. Mater. Interfaces. 8 (2016) 27632–27641. doi:10.1021/acsami.6b06456.

[60] J. W. Lee, T. Ahn, J. H. Kim, J. M. Ko, J. D. Kim, Nanosheets based mesoporous NiO microspherical structures via facile and template-free method for high performance supercapacitors, Electrochim. Acta. 56 (2011) 4849–4857. doi:10.1016/J.ELECTACTA.2011.02.116.

[61] A.G. Dylla, G. Henkelman, K.J. Stevenson, Lithium insertion in nanostructured TiO_2(B) architectures, Acc. Chem. Res. 46 (2013) 1104–1112. doi:10.1021/ar300176y.

[62] M.Q. Zhao, C.E. Ren, Z. Ling, M.R. Lukatskaya, C. Zhang, K.L. Van Aken, M.W. Barsoum, Y. Gogotsi, Flexible MXene/carbon nanotube composite paper with

high volumetric capacitance, Adv. Mater. 27 (2015) 339–345. doi:10.1002/adma.201404140.

[63] R.B. Rakhi, B. Ahmed, D. Anjum, H.N. Alshareef, Direct Chemical Synthesis of MnO_2 Nanowhiskers on Transition-Metal Carbide Surfaces for Supercapacitor Applications, ACS Appl. Mater. Interfaces. 8 (2016) 18806–18814. doi:10.1021/acsami.6b04481.

[64] P. Karthika, N. Rajalakshmi, K.S. Dhathathreyan, Functionalized Exfoliated Graphene Oxide as Supercapacitor Electrodes, 2 (2012) 59. doi:10.4236/SNL.2012.24011.

[65] G. Yu, L. Hu, N. Liu, H. Wang, M. Vosgueritchian, Y. Yang, Y. Cui, Z. Bao, Enhancing the supercapacitor performance of graphene/MnO_2 nanostructured electrodes by conductive wrapping, Nano Lett. 11 (2011) 4438–4442. doi:10.1021/nl2026635.

[66] G.S. Gund, D.P. Dubal, B.H. Patil, S.S. Shinde, C.D. Lokhande, Enhanced activity of chemically synthesized hybrid graphene oxide/Mn_3O_4 composite for high performance supercapacitors, Electrochim. Acta. 92 (2013) 205–215. doi:10.1016/j.electacta.2012.12.120.

[67] C. Zhang, K.B. Hatzell, M. Boota, B. Dyatkin, M. Beidaghi, D. Long, W. Qiao, E.C. Kumbur, Y. Gogotsi, Highly porous carbon spheres for electrochemical capacitors and capacitive flowable suspension electrodes, Carbon N. Y. 77 (2014) 155–164. doi:10.1016/j.carbon.2014.05.017.

[68] J.F. Marco, J.R. Gancedo, M. Gracia, J.L. Gautier, E.I. Rios, H.M. Palmer, C. Greaves, F.J. Berry, Cation distribution and magnetic structure of the ferrimagnetic spinel $NiCo_2O_4$, J. Mater. Chem. 11 (2001) 3087–3093. doi:10.1039/B103135J.

[69] G. Zhu, C. Xi, M. Shen, C. Bao, J. Zhu, Nanosheet-based hierarchical $Ni_2(CO_3)(OH)_2$ Microspheres with weak crystallinity for high-performance supercapacitor, ACS Appl. Mater. Interfaces. 6 (2014) 17208–17214. doi:10.1021/am505056d.

[70] Z.S. Wu, D.W. Wang, W. Ren, J. Zhao, G. Zhou, F. Li, H.M. Cheng, Anchoring hydrous RuO_2 on graphene sheets for high-performance electrochemical capacitors, Adv. Funct. Mater. 20 (2010) 3595–3602. doi:10.1002/adfm.201001054.

[71] Z.-S. Wu, W. Ren, D.-W. Wang, F. Li, B. Liu, H.-M. Cheng, High-Energy MnO_2 Nanowire/Graphene and Graphene Asymmetric Electrochemical Capacitors, ACS Nano. 4 (2010) 5835–5842. doi:10.1021/nn101754k.

[72] Q. Jiang, N. Kurra, M. Alhabeb, Y. Gogotsi, and H. N. Alshareef, All Pseudocapacitive MXene-RuO_2 Asymmetric Supercapacitors, Adv. Energy Mater. 8 (2018) 1703043. doi: 10.1002/aenm.201703043.

[73] H. Chen, L. Hu, Y. Yan, R. Che, M. Chen, L. Wu, One-step fabrication of ultrathin porous nickel hydroxide-manganese dioxide hybrid nanosheets for supercapacitor electrodes with excellent capacitive performance, Adv. Energy Mater. 3 (2013)

1636–1646. doi:10.1002/aenm.201300580.

[74] T. Chen, Y. Tang, Y. Qiao, Z. Liu, W. Guo, J. Song, S. Mu, S. Yu, Y. Zhao, F. Gao, All-solid-state high performance asymmetric supercapacitors based on novel MnS nanocrystal and activated carbon materials, Sci. Rep. 6 (2016) 23289. doi:10.1038/srep23289.

[75] A. Bergmann, I. Zaharieva, H. Dau, P. Strasser, Electrochemical water splitting by layered and 3D cross-linked manganese oxides: correlating structural motifs and catalytic activity, Energy Environ. Sci. 6 (2013) 2745. doi:10.1039/c3ee41194j.

[76] E. Raymundo-Piñero, P. Azaïs, T. Cacciaguerra, D. Cazorla-Amorós, A. Linares-Solano, F. Béguin, KOH and NaOH activation mechanisms of multiwalled carbon nanotubes with different structural organisation, Carbon N. Y. 43 (2005) 786–795. doi:10.1016/j.carbon.2004.11.005.

[77] J. Zhang, F. Liu, J.P. Cheng, X.B. Zhang, Binary Nickel-Cobalt Oxides Electrode Materials for High-Performance Supercapacitors: Influence of its Composition and Porous Nature, ACS Appl. Mater. Interfaces. 7 (2015) 17630–17640. doi:10.1021/acsami.5b04463.